Modular Four-Channel 50 kW WPT System With Decoupled Coil Design for Fast EV Charging

**HAO CHEN, ZHONGNAN QIAN, RUOQI ZHANG, (Graduate Student Member, IEEE),
ZHUHAOBO ZHANG, (Graduate Student Member, IEEE), JIANDE WU, (Member, IEEE),
HAO MA, (Senior Member, IEEE), AND XIANGNING HE, (Fellow, IEEE)**
College of Electrical Engineering, Zhejiang University, Hangzhou 310027, China

Corresponding author: Jiande Wu (eewjd@zju.edu.cn)

ABSTRACT High-power wireless power transfer (WPT) is an attractive option for fast charging of electric vehicles (EVs), but the power capability of the WPT system is limited by power devices and resonant elements. This paper presents a scalable modular four-channel WPT system for fast EV charging. Owing to the modular design, the four-channel system achieves 50 kW output power with low-power Silicon devices, and the reliability and robustness of the system are significantly improved. Through the coil structure and placement design, the four-channel magnetic coupler achieves inter-channel decoupling, eliminating interference between channels, simplifying control logic, and enabling scalable modular design. The four-channel magnetic coupler also has rotational symmetry, making the system have a balanced tolerance to misalignment in both lateral and vertical directions. The proposed magnetic coupler is verified by 3-D finite element method (FEM) simulation. A modular four-channel WPT prototype is built and tested. Experiments show that the prototype can deliver 50.8 kW to load with 97% dc-to-dc efficiency over a 200-mm airgap in aligned case, and has a balanced tolerance to misalignment in both the lateral and vertical directions.

INDEX TERMS Wireless electric vehicle (EV) charging, high-power, modular, decoupled coil design, misalignment tolerance.

I. INTRODUCTION

Nowadays, under the pressure of energy shortage and environmental pollution, the electric vehicle (EV) industry has achieved global expansion. However, there are still some significant challenges in EVs, e.g., EV batteries take a long time to charge compared with fueling a gasoline car [1], and traditional conductive charging of EV requires heavy gauge cables, which are difficult to handle and unsafe. As a substitute for conductive charging, wireless power transfer (WPT), mainly referring to inductive power transfer (IPT), has attracted a lot of attention in recent years due to the advantages of aesthetics, safety, convenience, and fully automated charging process [2]. However, WPT still faces the problem of long charging times especially in some practical applications, e.g., charging for public transport systems (buses and electric locomotives) [3]. High-power charging is the key to

reducing long charging times [4]. Therefore, the demand for high-power WPT is on the rise [3], [5], [6].

Due to the voltage and current limitations of power electronic devices, it is a big challenge to increase the power capability of WPT systems. Some commercial and academic institutions have proposed high-power WPT systems with a power level of 50 kW or higher [7]–[9], at the expense of using wide-bandgap devices such as Silicon-Carbide (SiC). But the further improvement of system power capability will still be limited by devices. In addition, in the case of the limited internal volume of EVs in practical application, the voltage stress and insulation of resonant elements are also the bottlenecks in the application of high-power wireless charging.

To address the above problem, various approaches have been proposed to circumvent the device and resonant element limitations to improve the power capability of WPT system. A cascaded multilevel inverter is proposed for the WPT system to improve the power level [10]–[13]. However, the cascaded structure of the multilevel converter suffers

TABLE 1. Designed index of modular four-channel WPT system.
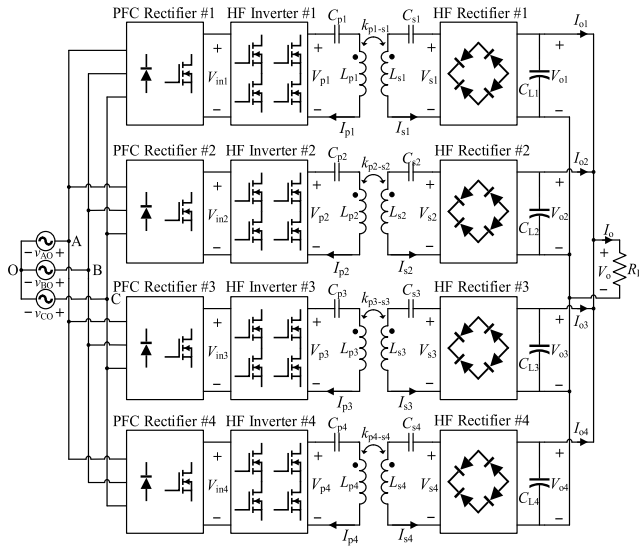
Symbol	Describe	Value
P_{total}	Rated total power	50 kW
$P_1 \sim P_4$	Single channel rated power	12.5 kW
$V_{in1} \sim V_{in4}$	Rated input DC voltage of primary side	800 V
V_o	Rated output DC voltage of secondary side	800 V
f_0	Operating frequency	85 kHz
H_{gap}	Air gap	200 mm

low reliability due to the series connection of the inverters. Multiple inverters with low-current semiconductor devices connected in parallel are proposed to increase the transmitter current and improve the reliability of WPT system [14]. However, the high transmitter current results in high voltage stress of the resonant elements, which makes insulation design more difficult. Both of the cascade and parallel connection methods mentioned above only adopt one transmitting coil, which results in only one power transfer channel in the system. They all face the problem of low reliability and malfunction when the fault occurs.

The WPT systems with multiple power transfer channels that consist of multiple transmitters and receivers are proposed in [15]–[19]. The system power capability is increased while the current stress of power devices and voltage stress of resonant elements are reduced. However, there is non-negligible cross-coupling between multiple power transfer channels, which causes unbalance power sharing and power circulation among channels, dramatically decreases the power transfer capability and efficiency [15]. In [17], the decoupling of two magnetic couplers is realized by the combination of polarized coils and nonpolarized coils. However, only 4.73 kW is transmitted in the two-channel system, and the method is not extendable so the transmission power capability cannot be further improved through modularization. In [18] and [19], altering the relative position of the two magnetic couplers made of polarized coils is utilized to eliminate the magnetic coupling between couplers. The two-channel systems are built with a transmission power of 44 kW and 7 kW respectively. The method is scalable, but further increases of modules will face the problem of low space utilization. In addition, due to the characteristics of polarized coils, the above-mentioned multi-channel systems suffer the imbalance of system misalignment tolerance in lateral and vertical directions, which increases the complexity of EVs parking in practical application.

In this paper, a modular four-channel WPT system with decoupled coil design is proposed for fast EV charging. The modular system contains four identical parallel power transfer channels, each of which is a complete WPT module, consisting of a primary PFC rectifier, an inverter, a pair of transmitter coil and receiver coil, and a secondary rectifier. Each module has the same power capability and the total transferred power is the sum of four modules. The contributions of this paper are summarized as follows.

1) Through the modular design, a 50-kW high-power WPT system is implemented using low-power silicon-based devices, and the voltage stress of the resonant elements is reduced. The four channels are identical and independent of each other, significantly enhancing the reliability and robustness of the system. Moreover, the modular design is scalable, the transmission power capability can be increased further by paralleling more modules.

2) A structure of an inter-channel decoupled four-channel magnetic coupler is proposed, which eliminates the interference between channels, simplifies control logic and allows for scalable modular design. Because the magnetic coupler also has rotational symmetry, the system has a balanced tolerance to misalignment in both the lateral and vertical directions.

3) The structure of the combination of Vienna PFC rectifier and cascaded dual full-bridge inverters is proposed to power the transmission coils, which further reduces the voltage stress of the power devices, for the voltage stress of the power device is only half of the DC bus voltage. When compared to the existing methods of using cascade inverters to achieve high power [1], [10], [11], [20], the output of the Vienna rectifier has a natural midpoint, and balanced input voltage of each inverter can be achieved.

This paper is organized as follows. In Section II, the structure of the modular four-channel WPT system is illustrated, and the input and output characteristics of the system are derived. In Section III, the four-channel decoupled magnetic coupler is designed, and its performance is analysed. In Section IV, the modular circuit is designed. In Section V, the experimental results for the verification of the proposed system are presented. In Section VI, the conclusions are given.
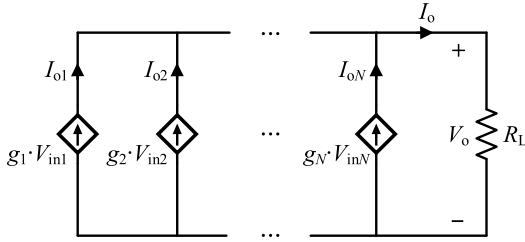
FIGURE 2. Equivalent circuit model of modular multi-channel WPT system.

FIGURE 3. (a) Magnetic field generated by nonpolarized coil. (b) Magnetic field generated by polarized coil.

II. MODULAR FOUR-CHANNEL WPT SYSTEM

The block diagram of the proposed modular four-channel WPT system is shown in Fig. 1, and the system parameters are shown in Table 1. The proposed system adopts input-parallel output-parallel (IPOP) topology, which consists of four identical WPT channels in parallel. Each channel is a complete WPT module that includes a grid side PFC rectifier, a primary side high-frequency inverter, compensation networks, and a secondary side high-frequency rectifier. More modules can be integrated to achieve higher power capability because the modular design is scalable. Following that, a generalized modular model with N channels will be developed (N is an arbitrary number).

The SS topology [21], [22] is adopted for compensation. Corresponding resonant conditions are given by

$$\omega_0 = 2\pi f_0 = \frac{1}{\sqrt{L_{pi}C_{pi}}} = \frac{1}{\sqrt{L_{si}C_{si}}} \quad (i = 1, 2, \ldots, N), \quad (1)$$

where ω_0 is the system frequency in rad/s. In accordance with SAE J2954 standard [23], the proposed system operating frequency f_0 is 85 kHz. The compensation networks can be compactly represented by matrixes given by

$$\begin{aligned}
\mathbf{L}_p &= \text{diag}[L_{p1}L_{p2}\ldots L_{pN}] \\
\mathbf{L}_s &= \text{diag}[L_{s1}L_{s2}\ldots L_{sN}] \\
\mathbf{C}_p &= \text{diag}[C_{p1}C_{p2}\ldots C_{pN}] \\
\mathbf{C}_s &= \text{diag}[C_{s1}C_{s2}\ldots C_{sN}],
\end{aligned} \quad (2)$$

$\mathbf{L}_p$ and $\mathbf{L}_s$ are multi-channel inductance matrixes, $\mathbf{C}_p$ and $\mathbf{C}_s$ are multi-channel capacitance matrixes. $\underline{\mathbf{Z}}_{Lp} = j\omega\mathbf{L}_p$, $\underline{\mathbf{Z}}_{Ls} = j\omega\mathbf{L}_s$, $\underline{\mathbf{Z}}_{Cp} = (j\omega\mathbf{C}_p)^{-1}$ and $\underline{\mathbf{Z}}_{Cs} = (j\omega\mathbf{C}_s)^{-1}$ are the impedance matrixes associated with the inductance and capacitance matrixes. The fundamental approximation is used to analyze the basic characteristics of the proposed modular topology. Ignoring high order harmonics, the multi-channel primary and secondary coil currents are given by the current vectors $\mathbf{I}_p = [I_{p1}\ I_{p2}\ldots I_{pN}]^T$ and $\mathbf{I}_s = [I_{s1}I_{s2}\ldots I_{sN}]^T$ respectively. The multi-channel output current and voltage are given by vectors $\mathbf{I}_o = [I_{o1}\ I_{o2}\ldots I_{oN}]^T$ and $\mathbf{V}_o = [V_{o1}V_{o2}\ldots V_{oN}]^T$ respectively. The input and output voltage of multi-channel inverters and the input voltage of the secondary rectifiers are given by vectors $\mathbf{V}_{in} = [V_{in1}V_{in2}\ldots V_{inN}]^T$, $\mathbf{V}_p = [V_{p1}V_{p2}\ldots V_{pN}]^T$, and $\mathbf{V}_s = [V_{s1}V_{s2}\ldots V_{sN}]^T$ respectively. Consider the cross-coupling between channels, the mutual inductance matrix $\mathbf{M}$
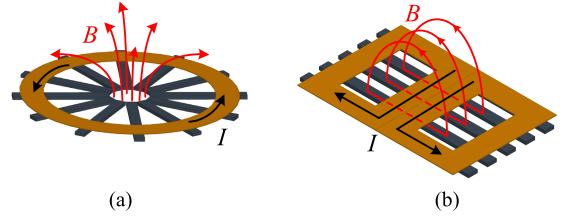
between multi-channel primary and secondary coils, and the equivalent load matrix $\underline{\mathbf{R}}_{ac}$ seen before secondary rectifiers are given by

$$\underline{\mathbf{M}}_{p-s} = \begin{bmatrix} M_{p1-s1} & M_{p1-s2} & \cdots & M_{p1-sN} \\ M_{p2-s1} & M_{p2-s2} & \cdots & M_{p2-sN} \\ \vdots & \vdots & \ddots & \vdots \\ M_{pN-s1} & M_{pN-s2} & \cdots & M_{pN-sN} \end{bmatrix} \quad (3)$$

$$\underline{\mathbf{M}}_{p-p} = \begin{bmatrix} 0 & M_{p1-p2} & \cdots & M_{p1-pN} \\ M_{p2-p1} & 0 & \cdots & M_{p2-pN} \\ \vdots & \vdots & \ddots & \vdots \\ M_{pN-p1} & M_{pN-p2} & \cdots & 0 \end{bmatrix} \quad (4)$$

$$\underline{\mathbf{M}}_{s-s} = \begin{bmatrix} 0 & M_{s1-s2} & \cdots & M_{s1-sN} \\ M_{s2-s1} & 0 & \cdots & M_{s2-sN} \\ \vdots & \vdots & \ddots & \vdots \\ M_{sN-s1} & M_{sN-s2} & \cdots & 0 \end{bmatrix} \quad (5)$$

$$\underline{\mathbf{R}}_{ac} = \text{diag}[R_{ac1}R_{ac2}\ldots R_{acN}]. \quad (6)$$

Using the fundamental approximation, define

$$\mathbf{V}_p = \frac{4}{\pi}\mathbf{V}_{in}, \quad \mathbf{V}_s = \frac{4}{\pi}\mathbf{V}_o. \quad (7)$$

From Fig. 1, Kirchhoff's voltage law gives

$$\mathbf{V}_p = (\underline{\mathbf{Z}}_{Lp} + \underline{\mathbf{Z}}_{Cp})\mathbf{I}_p + j\omega_0\underline{\mathbf{M}}_{p-s}\mathbf{I}_s + j\omega_0\underline{\mathbf{M}}_{p-p}\mathbf{I}_p \quad (8)$$

$$j\omega_0\underline{\mathbf{M}}_{p-s}\mathbf{I}_p + j\omega_0\underline{\mathbf{M}}_{s-s}\mathbf{I}_s = -(\underline{\mathbf{Z}}_{Ls} + \underline{\mathbf{Z}}_{Cs})\mathbf{I}_s - \underline{\mathbf{R}}_{ac}\mathbf{I}_s. \quad (9)$$

Substituting (1) into (8) and (9), then

$$\mathbf{V}_p = j\omega_0\underline{\mathbf{M}}_{p-s}\mathbf{I}_s + j\omega_0\underline{\mathbf{M}}_{p-p}\mathbf{I}_p \quad (10)$$

$$j\omega_0\underline{\mathbf{M}}_{p-s}\mathbf{I}_p + j\omega_0\underline{\mathbf{M}}_{s-s}\mathbf{I}_s = -\underline{\mathbf{R}}_{ac}\mathbf{I}_s. \quad (11)$$

The multi-channel secondary coil current vector can be calculated as

$$\mathbf{I}_s = \frac{\underline{\mathbf{M}}_{p-s}\mathbf{V}_p}{j\omega_0\underline{\mathbf{M}}_{p-s}^2 - (j\omega_0\underline{\mathbf{M}}_{p-p}\underline{\mathbf{M}}_{s-s} + \underline{\mathbf{M}}_{p-p}\underline{\mathbf{R}}_{ac})}. \quad (12)$$

In consideration of the rectifier bridge, the output dc current vector can be estimated as

$$\mathbf{I}_o = \frac{2\sqrt{2}}{\pi}\mathbf{I}_s. \quad (13)$$

Combining (7)(12) and (13), the output current of each channel can be expressed as

$$\mathbf{I}_o = \frac{8\sqrt{2}\mathbf{V}_{in}}{j\pi^2\omega_0\underline{\mathbf{M}}_{p-s} - (j\pi^2\omega_0\frac{\underline{\mathbf{M}}_{p-p}\underline{\mathbf{M}}_{s-s}}{\underline{\mathbf{M}}_{p-s}} + \frac{\underline{\mathbf{M}}_{p-p}}{\underline{\mathbf{M}}_{p-s}}\underline{\mathbf{R}}_{ac})} = \mathbf{GV}_{in}, \quad (14)$$
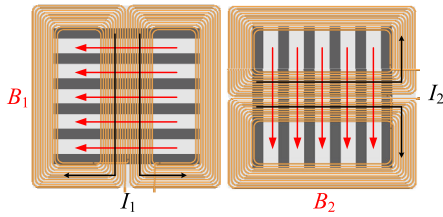
FIGURE 4. Orthogonal placement of two DD coils.

FIGURE 5. (a) Diagonal placement of two DD coils. (b) Simulated interference coupling coefficient with various rotating angle φ.

where $\underline{G}$ is the input to output gain matrix of multiple channels. From (14), when the cross-coupling between channels exists, the output of each channel is not independent but influenced by other channels, which affects the power transfer capacity and ZVS operation, and complicates the control logic. However, when the multi-channel system is inter-channel decoupling, $\underline{G}$ becomes a diagonal matrix, and each channel output operates as an independent current source. Therefore, the output of the multiple channels can be paralleled, and $V_{o1} = V_{o2} \ldots = V_{oN} = V_o$. Further, the proposed multi-channel WPT system can be expressed by the equivalent circuit model shown in Fig. 2. When each channel output is balanced as $I_{o1} = I_{o2} \ldots = I_{oN}$, the output power of the multi-channel system is

$$P_o = V_o I_o = V_o \left(I_{o1} + I_{o2} \ldots + I_{o4} \right), \quad (15)$$

and the equivalent DC load relationship of each channel is

$$R_{L1} = R_{L2} \ldots = R_{LN} = \frac{V_o}{I_o/N} = NR_L. \quad (16)$$

R_L is the actual load connected to the multi-channel system, and $R_{L1} \sim R_{LN}$ is the equivalent DC load of each channel.

From (15), the total transmission power capability of the four-channel system is four times that of the single-channel system. Therefore, it can be deduced that, under the same power level, the current stress of power devices of the four-channel system is one-quarter of that of the traditional single-channel system.

For high-power WPT applications such as fast EV charging, the modular design has the following advantages. First, compared with the single-channel structure, the four-channel structure at the same power level allows the use of low-power components, which are typically easier to realize, and the voltage stress of the resonant elements is relatively low. Second, increasing power level in a single-channel structure may necessitate a complete redesign of the power supply. In contrast, flexible power levels can be realized by paralleling different numbers of the module. Third, the four identical channels of the system can operate independently, significantly improving the reliability and robustness of the WPT system. Fourth, the modular structure simplifies the thermal design of the system, as the heat produced is more evenly dispersed.
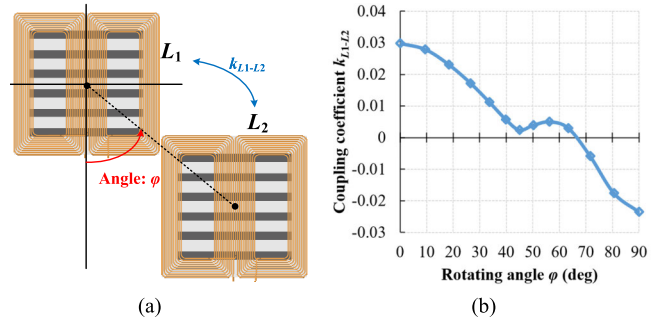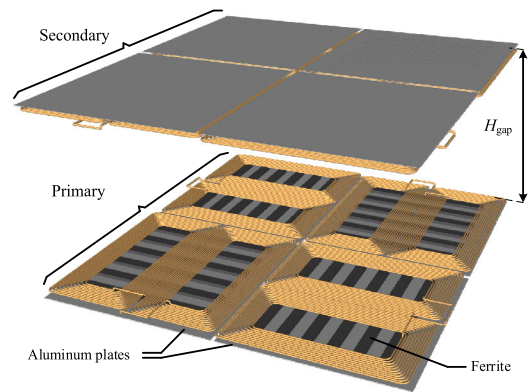

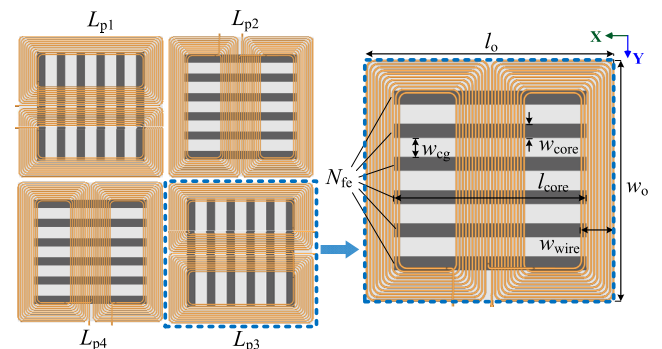**FIGURE 6.** Overall structure of the decoupled four-channel coupler.

FIGURE 7. Top view of the primary coils and structural parameters of a coil unit.

III. DESIGN OF FOUR-CHANNEL DECOUPLED COILS
A. COIL STRUCTURE SELECTION
In general, there are mainly two categories of coil structure for IPT systems, i.e., nonpolarized coil and polarized coil. Nonpolarized coil, such as circular coil and rectangular coil, generates the magnetic field scattered away from the center of the coil, as shown in Fig. 3(a). The magnetic field generated by polarized coils, such as solenoid coil and DD coil, is distributed along one dimension of the coil only, i.e., either length or width of the coil, as shown in Fig. 3 (b).

The multi-channel magnetic coupler consists of several single-channel magnetic couplers in restricted space. If a nonpolarized coil is utilized as the basic unit to construct a

TABLE 2. Structural parameters of DD coil unit.

Symbol	Describe	Value
l_o	Length of coil	600 mm
w_o	Width of coil	600 mm
N_{fe}	Number of ferrite plates	6
l_{core}	Length of ferrite cores	480 mm
w_{core}	Width of ferrite cores	35 mm
h_{core}	ferrite cores height	12 mm
w_{cg}	Ferrite cores gap	48 mm
w_{wire}	Wiring width of single winding	80 mm
-	Turns of coil	11

TABLE 3. Simulation results of coupling coefficient between primary coil L_{p1} and other 7 coils in aligned case.

$k_{p1\text{-}p2}$	$k_{p1\text{-}p3}$	$k_{p1\text{-}p4}$	$k_{p1\text{-}s1}$	$k_{p1\text{-}s2}$	$k_{p1\text{-}s3}$	$k_{p1\text{-}s4}$
0.004	0.008	0.004	0.261	0.004	0.007	0.004

multi-channel magnetic coupler, as the magnetic field generated by the nonpolarized coil is omnidirectional, no matter how to adjust the position of each channel coil, the magnetic field of each channel will inevitably cross-link, the inter-channel decoupling cannot be realized. Therefore, the design of the multi-channel decoupling coupler requires the polarized coil as the basic unit. In this paper, the DD coil is selected as the geometry of the coil unit owing to its higher power transfer height for a given coil diameter and current [24].

B. PLACEMENT OF FOUR-CHANNEL DECOUPLED COILS

In recent years, many approaches have been reported to eliminate the interference coupling between channels by designing the placement of two polarized coils. In [19], three types of relative position between two DD coils are analyzed, which shows that orthogonal placement has the minimum cross-coupling compared with lateral placement or vertical placement, but the diagonal placement of DD coils is not considered. In [18], the diagonal placement of the two sets of solenoid coils is proposed to reduce the interference coupling. The relationship between the rotating angle of the two sets of coils and interference coupling is simulated, which indicates that in a certain rotating angle, the interference coupling is inverted from positive to negative and zero-cross. The diagonal placement of DD coils has similar characteristics, which are verified below.

The diagram of the diagonal placement of two DD coils is shown in Fig. 5(a). The positions of the two coils are rotated while keeping the direction of the coils parallel and the edges close. The rotating angle φ is defined in Fig. 5(a). The coupling coefficient between the two coils is simulated by 3-D finite element method (FEM). The relationship between various rotating angles φ and the simulated interference coupling coefficient is shown in Fig. 5(b). The interference coupling between the two coils corresponds to k_{L1-L2}. The simulation results show that the k_{L1-L2} is inverted from

positive to negative and zero-cross when the rotating angle φ is between 60 to 70 degrees, and the k_{L1-L2} is approximately zero when φ is 45 degrees. To utilize the zero point (or the point close to zero) of the interference coupling, decoupling between diagonally placed two DD coils can be realized.
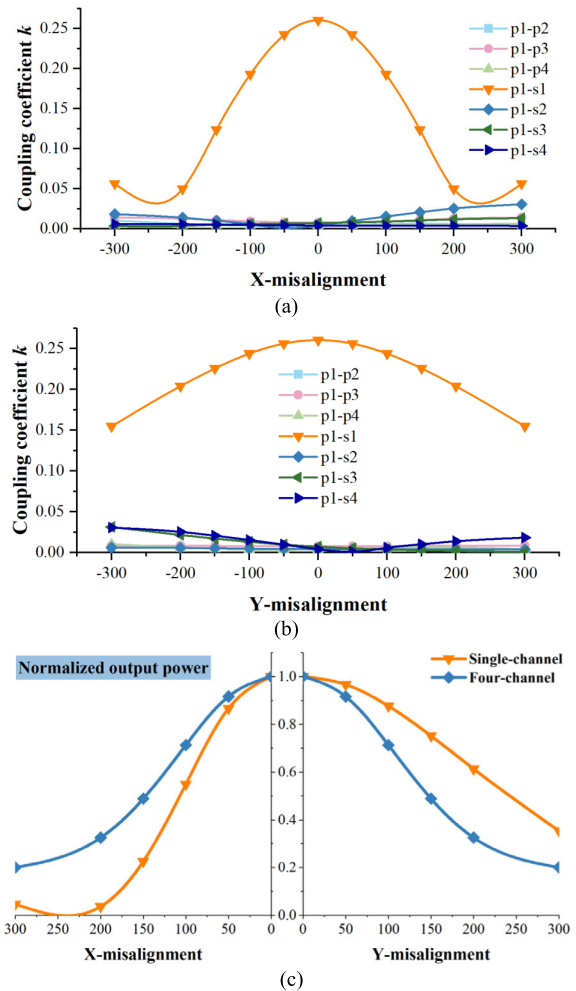

FIGURE 8. Simulation results of four-channel magnetic coupler misalignment. (a) (b) Coupling coefficient between primary coil L_{p1} and other 7 coils. (c) Comparison of normalized system output power under different misalignment conditions between single-channel and four-channel system (in the case of the same primary coil current).

Comprehensive consideration of the two placement methods and space utilization, the placement of four-channel magnetic coupler with inter-channel decoupling is proposed, which integrates the orthogonal placement and the diagonal placement. The overall structure of the designed decoupled four-channel magnetic coupler is shown in Fig. 6, in which the secondary side coil and ferrite part covered by aluminum plates are completely the same as the primary side. The top view of the primary coils is shown in Fig. 7. It can be seen that the coupling structure uses the DD coil as the basic unit, and the four DD coils correspond to the four-primary inductance $L_{p1} \sim L_{p4}$ in Fig. 1. Specifically, adjacent coils are placed orthogonal (such as L_{p1} and L_{p2}). Non-adjacent
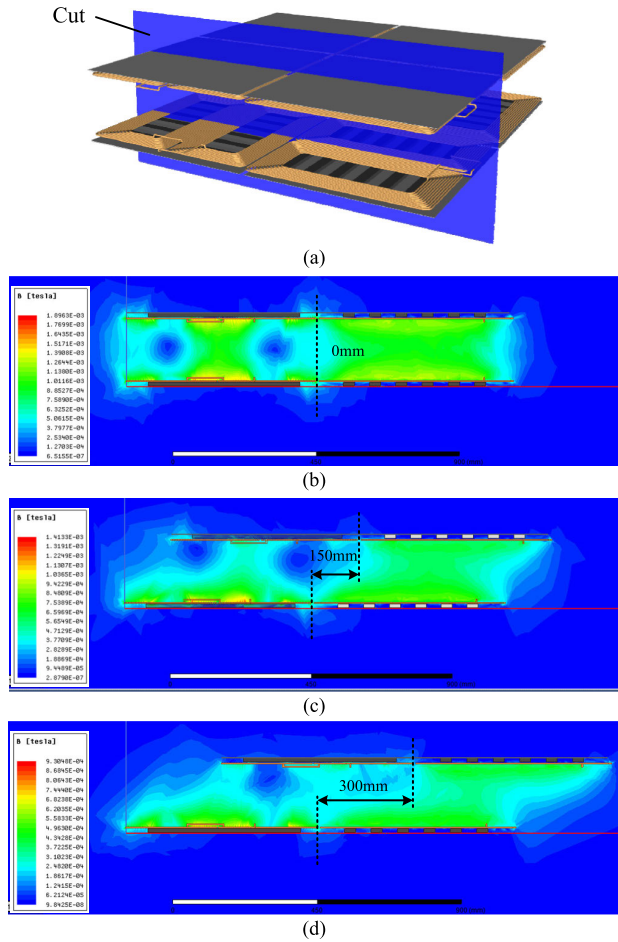
(a)

(b)

(c)

(d)

FIGURE 9. Magnetic field distributions of the magnetic coupler under different misalignment conditions. (a) Definition of the cut surface. (b) Fully aligned. (c) X/Y-misalignment = 150 mm. (d) X/Y-misalignment = 300 mm.

coils are placed parallelly and diagonally, with a rotating angle φ of 45 degrees (such as L_{p1} and L_{p3}). Thus, the inter-channel decoupling of the four-channel magnetic coupler is realized while space utilization is maximized. The structural parameters of the DD coil unit are listed in Table 2, and the corresponding parameters are shown in Fig. 7.

C. SIMULATION OF COUPLING COEFFICIENT AND MISALIGNMENT

To verify the inter-channel decoupling of the proposed four-channel magnetic coupler, the simulation is conducted by 3-D FEM. Since there are 8 inductive coils ($L_{p1} \sim L_{p4}$ and $L_{s1} \sim L_{s4}$) in the four-channel magnetic coupler, totaling 28 coupling coefficients can be formed, including four coupling coefficients k_{p1-s1}, k_{p2-s2}, k_{p3-s3}, and k_{p4-s4} for power transmission, 24 interference coupling coefficients k_{pi-sj}, k_{pi-pj}, and k_{si-sj} ($i \neq j$). When the primary and secondary sides of the magnetic coupler are horizontally aligned and the air gap H_{gap} is 200 mm, the simulation results of the coupling coefficients between the primary coil L_{p1} and the other 7 coils are shown in Table 3. Since the proposed magnetic coupler is

symmetrical about the center, all the 28 coupling coefficients in the magnetic coupler can be expressed by the 7 coupling coefficients of the primary coil L_{p1}.

The simulation results in Table 3 show that when the primary and secondary sides are horizontally aligned, the coupling coefficient k_{p1-s1} for power transmission is 0.261, while the six interference coupling coefficients between the channels are two orders of magnitude smaller than k_{p1-s1}, approximately zero. Therefore, the inter-channel decoupling of the designed four-channel magnetic coupler is realized under aligned condition.

The misalignment performance of the proposed four-channel magnetic coupler is analyzed too. The simulation results in Fig. 8 (a) and (b) show the coupling coefficient between primary coil L_{p1} and other 7 coils under different misalignment conditions. Due to the structural characteristics of DD coupler, a zero-coupling point is provided in lateral direction (X-axis) at an offset of approximately 34% of the coil dimension [25]. For the single-channel coupler, the anti-misalignment performance in vertical direction (Y-axis) is much better than that in lateral direction (X-axis). When the lateral (X-axis) misalignment reaches 200 mm, the coupling coefficient for power transmission drops sharply to almost zero. Under this condition, the traditional single-channel system with DD coils is unable to carry out effective power transmission.

To compare the misalignment performance between four-channel magnetic coupler and single-channel coupler, the system output power in misalignment conditions is analyzed by simulation. It should be noted that due to the characteristics of the SS topology, when misalignment occurs, the coupling coefficient decreases, and the power coil current will increase, which may exceed the current capacity of the coil. Therefore, the output power of the system is measured in the case of the same primary coil current in aligned condition. Actually, the output power is decreased under these conditions. It can be deduced from Fig. 6 that through the design of four-channel coils placement, the magnetic coupler has rotational symmetry and the rotation angle is 90 degrees. Therefore, the proposed four-channel magnetic coupler has the same tolerance to misalignment in both the lateral direction (X-axis) and vertical direction (Y-axis), as shown in Fig. 8 (c). The simulation results demonstrate that compared with the traditional single-channel system with DD coils, the proposed modular four-channel system has a balanced tolerance to misalignment in both the lateral and vertical directions.

The operating performance of the designed four-channel magnetic coupler is verified by joint simulation of 3-D FEM and ANSYS Simplorer. The magnetic field around the four-channel coils is calculated. Owing to the rotational symmetry of the four-channel magnetic coupler, the operating conditions of each channel can be expressed by the magnetic field distribution around the two adjacent channel coils. A 2-D cut surface is defined in the 3-D model of the four-channel coils, as shown in Fig. 9(a). The magnetic field on the
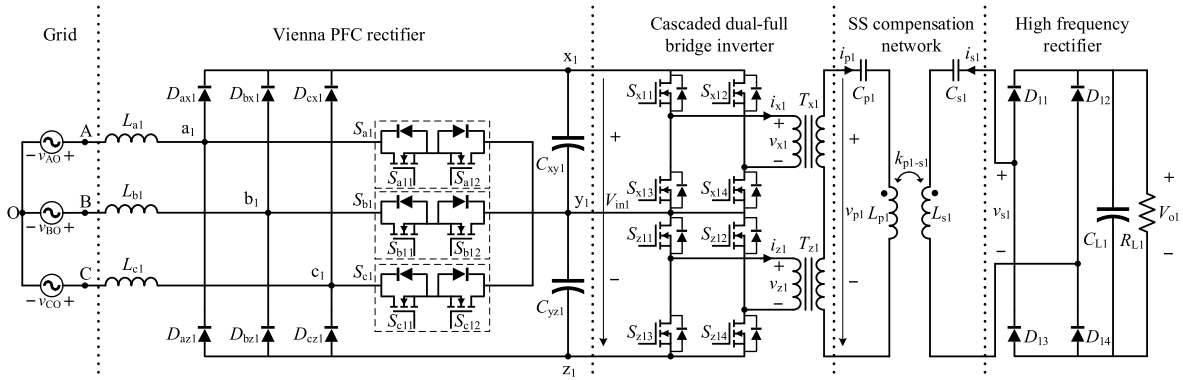
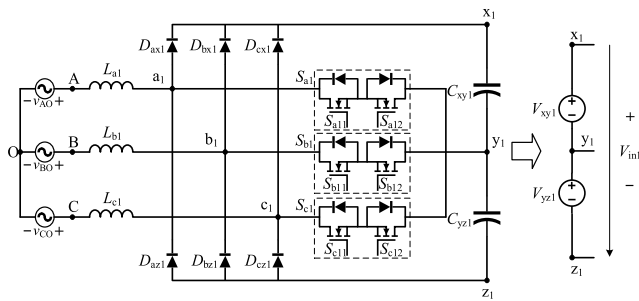**FIGURE 10.** Schematic diagram of the circuit module.

FIGURE 11. Output equivalent model of Vienna rectifier.

cut surface under different misalignment conditions is shown in Fig. 9(b)(c)(d). It can be seen that with the increase of misalignment, the delivered power of the channel on the left is significantly decreased, while the delivered power of the channel on the right remains high, which agrees well with the theoretical analysis.

IV. MODULAR CIRCUIT DESIGN

As shown in Fig. 1, each channel of the proposed four-channel WPT system has a circuit module with the same specifications. The circuit module includes a grid-side PFC rectifier, a primary side high-frequency inverter, compensation networks, and a secondary side high-frequency rectifier. Taking Channel 1 as an example, the schematic diagram of the circuit module is shown in Fig. 10.

A. GIRD-SIDE PFC RECTIFIER

The grid-side rectifier is Vienna rectifier. Vienna rectifier has the characteristics of small passive components scale, high power density, and high rectification efficiency [26]. The voltage stress of the rectifier power device is half of its output DC voltage (V_{in1} in Fig. 10), which allows the rectifier to achieve a higher DC voltage output. For the later stage circuit, the high-voltage DC bus is beneficial to minimize power coil current. When the quality factor of the power coil is set, it will decrease the loss of the power coil and improve the efficiency of energy transmission.

The discussion on the working principle and control method of Vienna rectifier is beyond the research scope of this paper. To facilitate the discussion of the post-stage circuit, the output of Vienna rectifier can be equivalent to two series DC voltage sources of equal amplitude, as shown in Fig. 11, and the voltage relationship follows

$$V_{xy1} = V_{yz1} = \frac{1}{2}V_{in1}. \tag{17}$$

B. PRIMARY SIDE HIGH-FREQUENCY INVERTER

In the proposed modular four-channel system, the current capacity of power devices in the inverter is one-quarter of that of the single-channel system at the same power level. To reduce the voltage stress of the devices at the same time, a cascaded dual-full bridge inverter is adopted, as shown in Fig. 10. The input sources of the two full-bridge inverters are the DC sources V_{xy1} and V_{yz1} in Fig. 11, which is half of the DC bus voltage V_{in1}. The cascaded design reduces the voltage stress of power devices to half that of the traditional full-bridge inverter. Therefore, for the 800 V DC bus voltage, the 650 V withstand voltage silicon-based MOSFET can be used in both Vienna rectifier and inverter as a cost-effective option.

Generally, SiC devices are required for a single inverter to achieve an input and output voltage level of 800 V. In this paper, the same voltage level can be achieved by Si devices through the combination of Vienna rectifier and cascaded inverter. In addition, with the combination of Vienna PFC rectifier and cascaded dual full-bridge inverters, the balanced input voltage of each inverter is be achieved because the output of the Vienna rectifier has a natural midpoint, compared with the existing methods of using cascade inverters to achieve high power, the problem of device damage caused by inconsistent voltage stress of the switching devices of the inverter is avoided.

Since the two input voltage sources V_{xy1} and V_{yz1} of the cascaded dual-full bridge inverter are not two isolated sources, they have a common point y_1, so the output of the upper and lower inverter cannot be cascaded directly, but are cascaded by the high-frequency transformers T_{x1} and T_{z1}

(turn ratio 1:1). Otherwise, in certain switching states, the DC voltage sources V_{xy1} and V_{yz1} would be short-circuited. The use of the high-frequency transformers also benefits the electrical isolation between the inverter and the post-stage circuit.

The switch driving signals of the two full-bridge inverters are set to be consistent. Thus, the output voltage v_{p1} of the cascaded dual-full bridge inverter is equal to twice the output voltage v_{x1} or v_{z1} of a single full-bridge inverter.

$$v_{p1} = 2v_{x1} = 2v_{z1} \tag{18}$$
$$i_{p1} = i_{x1} = i_{z1} \tag{19}$$

IPW65R080CFD 650 V/27 A silicon-based MOSFET from Infineon is selected for the Vienna rectifier and cascaded dual-full bridge inverter. For half of the maximum DC bus voltage of 400 V, the rated 650 V of the device has sufficient margin. In particular, two parallel-connected devices with 80 mΩ ON-state resistance in TO-247 housings are used for each switch of the dual-full bridge inverter in order to achieve low conduction losses.

V. EXPERIMENTAL VERIFICATION

The prototype of the proposed modular four-channel 50 kW WPT system is shown in Fig. 12. The prototype of the Vienna rectifier and the cascaded dual-full bridge inverter is shown in Fig. 13(a) and Fig. 13 (b). The designed DD coils with parameters corresponding to Table 2 are assembled and shown in Fig. 13(c). For the permeability and the Steinmetz parameters of the cores, the ferrite material PC95 is considered. A litz wire comprising 1600×0.1 mm strands and outer diameter $d_a = 5$ mm is used for the winding of the coils, the recommended current of the litz wire is 47.2 A (@50 kHz-100 kHz) [27]. Compensation capacitors should be chosen based on voltage and current ratings, as well as dimensions. Because of their good thermal stability, low impact of humidity on capacitance value, and excellent loss characteristics up to high frequencies, high-power polypropylene film capacitors of type DTR with custom capacitance values are used. According to the manufacturer, the dissipation factor of these devices is 1×10^{-4} (@100 kHz) [28]. The prototype parameters are shown in Table 4.

Taking Channel 1 as an example, the experimental waveform when Channel 1 is fully loaded is shown in Fig. 14. v_{x1} and v_{z1} are the output voltage of the upper and lower inverter of the cascaded dual-full bridge inverter respectively, i_{x1} is the output current of the upper inverter, V_{o1} is the output voltage of the secondary side. The inverter input voltage V_{in1} is 750 V, and the load is the single-channel rated load $R_{L1} = 42$ Ω. It can be seen that the output voltage v_{x1} of the upper inverter is the same as the output voltage v_{z1} of the lower inverter. The peak value of i_{x1} is 30 A, and the phase of v_{x1} (v_{z1}) is slightly ahead of i_{x1} (i_{z1}), so the ZVS is realized. The secondary output voltage V_{o1} is 736 V and the Channel 1 output power is 12.9 kW. The system dc-to-dc transmission
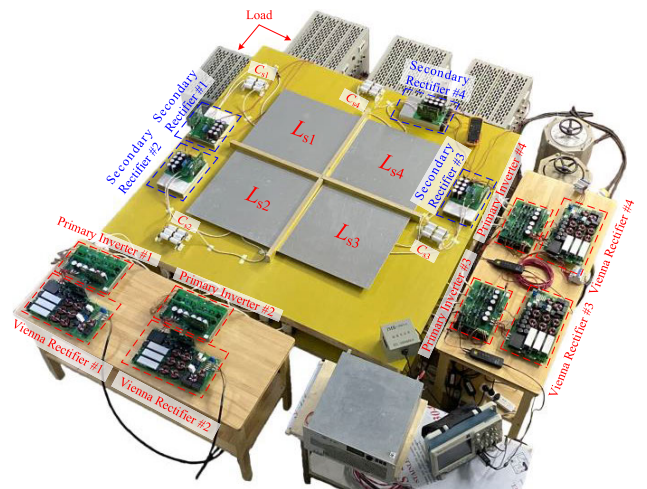

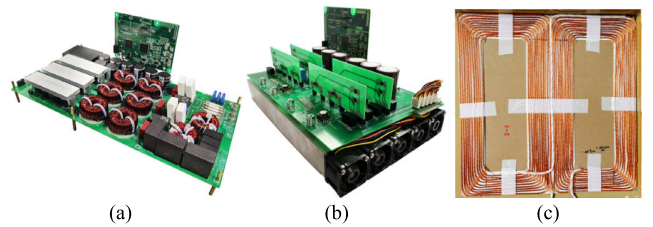**FIGURE 12.** The prototype of modular four-channel 50 kW WPT system.

(a)   (b)   (c)

FIGURE 13. The prototype. (a) Vienna rectifier. (b) Cascaded dual-full bridge inverter. (c) DD coil.

TABLE 4. The prototype parameters.

Compensation network			
Symbol	Value	Symbol	Value
L_{p1}	270.4 uH	C_{p1}	12.5 nF
L_{p2}	273.7 uH	C_{p2}	14.0 nF
L_{p3}	271.7 uH	C_{p3}	12.9 nF
L_{p4}	279.5 uH	C_{p4}	13.5 nF
L_{s1}	274.8 uH	C_{s1}	13.1 nF
L_{s2}	271.9 uH	C_{s2}	13.5 nF
L_{s3}	274.9 uH	C_{s3}	13.0 nF
L_{s4}	269.6 uH	C_{s4}	13.1 nF
$k_{p1\text{-}s1}$	0.234	$k_{p3\text{-}s3}$	0.235
$k_{p2\text{-}s2}$	0.235	$k_{p4\text{-}s4}$	0.235
System power and load			
System rated output power		50 kW	
Single channel load R_{L1}-R_{L4}		42 Ω	
Four-channel load R_L		10.5 Ω	

efficiency is expressed as

$$\eta = \frac{P_{out}}{P_{in}} = \frac{V_o \sum_{i=1}^{4} I_{oi}}{\sum_{i=1}^{4} V_{ini} I_{ini}}. \tag{20}$$

The measured single-channel efficiency is 97.2%.

The experimental waveform when the four channels are fully loaded is shown in Fig. 15. i_{x2}, i_{x3}, and i_{x4} are the upper inverter output current of Channel 2 ∼ 4 respectively, V_o is the output voltage of the four-channel system. The input voltage V_{in1} ∼ V_{in4} of the four channels are all 750 V, and the load is four-channel rated load $R_L = 10.5$ Ω. Due to the limited
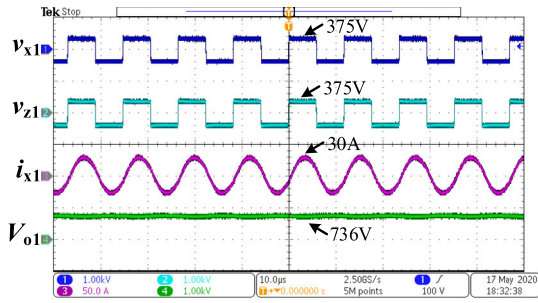
FIGURE 14. Waveform when single channel is fully loaded (single-channel load R_{L1} = 42 Ω).
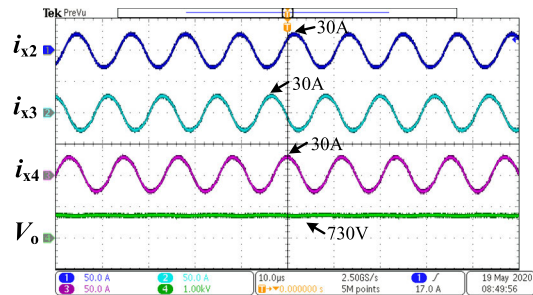

FIGURE 15. Waveform when four channels are fully loaded (four-channel load R_L = 10.5 Ω).
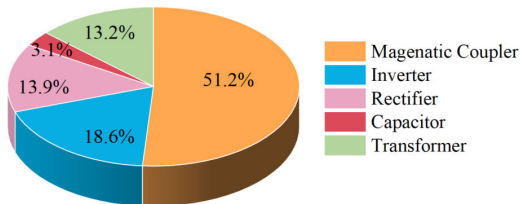

FIGURE 16. Calculated power loss contributions to the total losses of the system prototype.

measurement channels of the oscilloscope, the upper inverter output current i_{x1} of Channel 1 is not shown in Fig. 15, yet the waveforms and amplitudes of i_{x1} and i_{x2}, i_{x3}, i_{x4} are almost the same, only the phases are slightly different (the phases of the four channels are not synchronized). Due to the tolerance between the components and coils, the four-channel output voltage is slightly different from that of the single-channel, which is 730 V, and the output power is 50.8 kW. The measured dc-to-dc transmission efficiency is 97.0%, and the calculated power loss distribution is shown in Fig. 16.

The experiments of the four-channel system under misalignment conditions are taken too. The same as the simulation setting, in order to ensure that the coil current does not exceed the coil current capacity, the output power of the system here is measured in the case of the same primary coil current of 30 A (peak) in aligned condition. Therefore, the output power is decreased under misalignment conditions. The experimental results of each channel output power under different misalignment conditions are shown in Fig. 17.
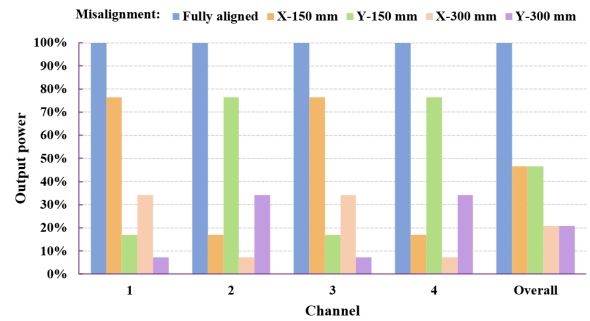

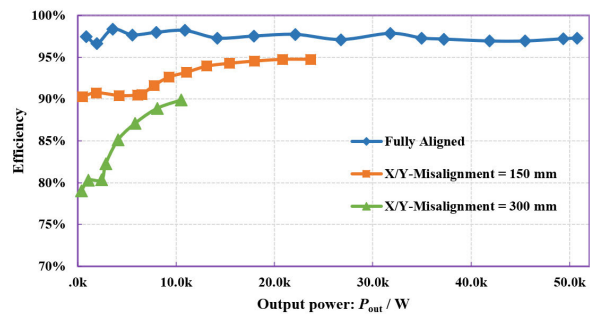**FIGURE 17.** Normalized system output power under different misalignment conditions.

FIGURE 18. System output power and efficiency.

To facilitate the display, normalized processing is adopted. It can be seen that for the single channel, the tolerance to misalignment in the lateral (X-axis) and vertical direction (Y-axis) is imbalanced. While for the four-channel system, the tolerance to misalignment is balanced in the lateral and vertical directions.

The experimental results of the relationship between system output power and efficiency are shown in Fig. 18. It can be seen that under aligned condition, the efficiency is almost unchanged during the entire power range. Under the misalignment condition, the maximum power transferability and the system efficiency are reduced with the misalignment increase. Under the same misalignment condition, the efficiency is improved with the increase of transfer power. When a 150 mm lateral or vertical misalignment occurs, the system's maximum output power drops to 23.7 kW with an efficiency of 94.8%. When a 300 mm lateral or vertical misalignment occurs, the system's maximum output power drops to 10.5 kW with an efficiency of 89.9%.

VI. CONCLUSION

This paper proposes a modular four-channel 50 kW WPT system with decoupled coil design for fast EV charging. Owing to the proposed scalable modular design, the system achieves 50-kW output power with low-power Silicon devices, significantly enhancing the reliability and robustness of the system. The transmission power capability can be further increased by adding more modules. Through the selection of coil structure and design of four-channel coils

placement, the magnetic coupler of the four-channel system achieves inter-channel decoupling, thereby minimizing channel interference, simplifying control logic, and enabling a scalable modular design. Additionally, the magnetic coupler is constructed with rotational symmetry, which provides a balanced tolerance for misalignment in both the lateral and vertical directions. The proposed magnetic coupler design is verified by 3-D FEM simulation. A four-channel WPT prototype is built to verify the proposed system. The experimental results demonstrated that the proposed modular four-channel WPT system can deliver 50.8 kW to the load with 97% dc-to-dc efficiency over a 200-mm airgap in the aligned case, and has a balanced tolerance to misalignment in both the lateral and vertical directions.

However, when compared to the conventional single channel WPT, this method reduces the cost of switching devices but increases the cost of other elements (controllers, coils, magnetic cores). Additionally, the coil power density is relatively low, with a total transmission capacity of just 50 kW via four pairs of 600mm * 600mm coils, so the approach is only suited to large vehicles such as buses. It can be further investigated to increase coil power density, and reduce EMI emission via multi-channel synchronous control.

REFERENCES

[1] D. Patil, M. K. McDonough, J. M. Miller, B. Fahimi, and P. T. Balsara, "Wireless power transfer for vehicular applications: Overview and challenges," *IEEE Trans. Transport. Electrific.*, vol. 4, no. 1, pp. 3–37, Mar. 2018.

[2] T. Trigg, P. Telleen, R. Boyd, F. Cuenot, D. D'Ambrosio, R. Gaghen, J. F. Gagné, A. Hardcastle, D. Houssin, A. R. Jones, and H. Kaneko, "Global EV outlook: Understanding the electric vehicle landscape to 2020," *Int. Energy Agency*, vol. 1, pp. 1–40, Apr. 2013.

[3] J. H. Kim, B.-S. Lee, J.-H. Lee, S.-H. Lee, C.-B. Park, S.-M. Jung, S.-G. Lee, K.-P. Yi, and J. Baek, "Development of 1-MW inductive power transfer system for a high-speed train," *IEEE Trans. Ind. Electron.*, vol. 62, no. 10, pp. 6242–6250, Oct. 2015.

[4] A. Foote and O. C. Onar, "A review of high-power wireless power transfer," in *Proc. IEEE Transp. Electrific. Conf. Expo (ITEC)*, Chicago, IL, USA, Jun. 2017, pp. 234–240.

[5] J. M. Miller and A. Daga, "Elements of wireless power transfer essential to high power charging of heavy duty vehicles," *IEEE Trans. Transport. Electrific.*, vol. 1, no. 1, pp. 26–39, Jun. 2015.

[6] H. Hao, G. A. Covic, and J. T. Boys, "A parallel topology for inductive power transfer power supplies," *IEEE Trans. Power Electron.*, vol. 29, no. 3, pp. 1140–1151, Mar. 2014.

[7] J. Pries, V. P. N. Galigekere, O. C. Onar, and G.-J. Su, "A 50-kW three-phase wireless power transfer system using bipolar windings and series resonant networks for rotating magnetic fields," *IEEE Trans. Power Electron.*, vol. 35, no. 5, pp. 4500–4517, May 2020.

[8] V. P. Galigekere, J. Pries, O. C. Onar, G.-J. Su, S. Anwar, R. Wiles, L. Seiber, and J. Wilkins, "Design and implementation of an optimized 100 kW stationary wireless charging system for EV battery recharging," in *Proc. IEEE Energy Convers. Congr. Expo. (ECCE)*, Portland, OR, USA, Sep. 2018, pp. 3587–3592.

[9] R. Bosshard and J. W. Kolar, "Multi-objective optimization of 50 kW/85 kHz IPT system for public transport," *IEEE J. Emerg. Sel. Topics Power Electron.*, vol. 4, no. 4, pp. 1370–1382, Dec. 2016.

[10] Y. Li, R. Mai, M. Yang, and Z. He, "Cascaded multi-level inverter based IPT systems for high power applications," *J. Power Electron.*, vol. 15, no. 6, pp. 1508–1516, Nov. 2015.

[11] B. X. Nguyen, D. M. Vilathgamuwa, G. Foo, A. Ong, P. K. Sampath, and U. K. Madawala, "Cascaded multilevel converter based bidirectional inductive power transfer (BIPT) system," in *Proc. Int. Power Electron. Conf. (IPEC-Hiroshima, ECCE ASIA)*, Hiroshima, Japan, May 2014, pp. 2722–2728.

[12] H. R. Rahnamaee, U. K. Madawala, and D. J. Thrimawithana, "A multilevel converter for high power-high frequency IPT systems," in *Proc. IEEE 5th Int. Symp. Power Electron. Distrib. Gener. Syst. (PEDG)*, Galway, Ireland, Jun. 2014, pp. 1–6.

[13] H. R. Rahnamaee, D. J. Thrimawithana, and U. K. Madawala, "MOSFET based multilevel converter for IPT systems," in *Proc. IEEE Int. Conf. Ind. Technol. (ICIT)*, Busan, South Korea, Feb. 2014, pp. 295–300.

[14] Q. Deng, P. Sun, W. Hu, D. Czarkowski, M. K. Kazimierczuk, and H. Zhou, "Modular parallel multi-inverter system for high-power inductive power transfer," *IEEE Trans. Power Electron.*, vol. 34, no. 10, pp. 9422–9434, Oct. 2019.

[15] D. Ahn and S. Hong, "Effect of coupling between multiple transmitters or multiple receivers on wireless power transfer," *IEEE Trans. Ind. Electron.*, vol. 60, no. 7, pp. 2602–2613, Jul. 2013.

[16] R. Johari, J. V. Krogmeier, and D. J. Love, "Analysis and practical considerations in implementing multiple transmitters for wireless power transfer via coupled magnetic resonance," *IEEE Trans. Ind. Electron.*, vol. 61, no. 4, pp. 1774–1783, Apr. 2014.

[17] Y. Li, T. Lin, R. Mai, L. Huang, and Z. He, "Compact double-sided decoupled coils-based WPT systems for high-power applications: Analysis, design, and experimental verification," *IEEE Trans. Transport. Electrific.*, vol. 4, no. 1, pp. 64–75, Mar. 2018.

[18] T. Shijo, K. Ogawa, M. Suzuki, Y. Kanekiyo, M. Ishida, and S. Obayashi, "EMI reduction technology in 85 kHz band 44 kW wireless power transfer system for rapid contactless charging of electric bus," in *Proc. IEEE Energy Convers. Congr. Expo. (ECCE)*, Milwaukee, WI, USA, Sep. 2016, pp. 1–6.

[19] H. Liu, Q. Chen, G. Ke, X. Ren, and S.-C. Wong, "Research of the input-parallel output-series inductive power transfer system," in *Proc. IEEE PELS Workshop Emerg. Technol., Wireless Power (WoW)*, Daejeon, South Korea, Jun. 2015, pp. 1–7.

[20] E. Babaei and S. H. Hosseini, "New cascaded multilevel inverter topology with minimum number of switches," *Energy Convers. Manage.*, vol. 50, no. 11, pp. 2761–2767, Nov. 2009.

[21] C.-S. Wang, G. A. Covic, and O. H. Stielau, "Power transfer capability and bifurcation phenomena of loosely coupled inductive power transfer systems," *IEEE Trans. Ind. Electron.*, vol. 51, no. 1, pp. 148–157, Feb. 2004.

[22] G. B. Joun and B. H. Cho, "An energy transmission system for an artificial heart using leakage inductance compensation of transcutaneous transformer," *IEEE Trans. Power Electron.*, vol. 13, no. 6, pp. 1013–1022, Nov. 1998.

[23] *Wireless Power Transfer for Light-Duty Plug-in/Electric Vehicles and Alignment Methodology*, Standard J2954_202010, 2020. [Online]. Available: https://saemobilus.sae.org/content/j2954_202010

[24] A. Ahmad, M. S. Alam, and R. Chabaan, "A comprehensive review of wireless charging technologies for electric vehicles," *IEEE Trans. Transport. Electrific.*, vol. 4, no. 1, pp. 38–63, Mar. 2018.

[25] N. Liu and T. G. Habetler, "Design of a universal inductive charger for multiple electric vehicle models," *IEEE Trans. Power Electron.*, vol. 30, no. 11, pp. 6378–6390, Nov. 2015.

[26] J. W. Kolar and F. C. Zach, "A novel three-phase utility interface minimizing line current harmonics of high-power telecommunications rectifier modules," *IEEE Trans. Ind. Electron.*, vol. 44, no. 4, pp. 456–467, Aug. 1997.

[27] Gucien Electric. *LW1600/0.10S2.0M33 Data Sheet*. Accessed: Aug. 21, 2022. [Online]. Available: http:///www.gucien.com

[28] Dawn Electronic. *DTR Series Resonance Capacitor Data Sheet*. Accessed: Aug. 21, 2022. [Online]. Available: http:///www.dawn-cap.cn
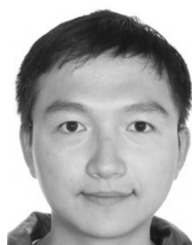
HAO CHEN received the B.Sc. degree in electrical engineering from Zhejiang University, Hangzhou, China, in 2019, where he is currently pursuing the M.Sc. degree with the College of Electrical Engineering.

His current research interests include wireless power transfer, foreign object detection, and position detection for inductive power transfer systems.

ZHONGNAN QIAN received the B.Sc. and Ph.D. degrees in electrical engineering from Zhejiang University, Hangzhou, China, in 2014 and 2020, respectively.

His current research interests include wireless power transfer and communication techniques applied in power electronics.

RUOQI ZHANG (Graduate Student Member, IEEE) received the B.S. degree in electrical engineering from Zhejiang University, Hangzhou, China, in 2016, where he is currently pursuing the Ph.D. degree with the College of Electrical Engineering.

From September 2015 to June 2016, he was an Intern with Silan Microelectronics Company Ltd., Hangzhou. His current research interest includes communication techniques applied in distributed power electronics systems.

ZHUHAOBO ZHANG (Graduate Student Member, IEEE) received the B.S. degree in electrical engineering from Zhejiang University, Hangzhou, China, in 2017, where he is currently pursuing the Ph.D. degree in electrical engineering.

His main research interests include wireless power transfer, resonant converters, and electric vehicle charging systems.

JIANDE WU (Member, IEEE) was born in Zhejiang, China, in 1973. He received the B.Sc., M.Sc., and Ph.D. degrees from the College of Electrical Engineering, Zhejiang University, Hangzhou, China, in 1994, 1997, and 2012, respectively.

Since 1997, he has been a Faculty Member at Zhejiang University, where he is currently an Associate Professor. From 2013 to 2014, he was an Academic Visitor at the University of Strathclyde, Glasgow, U.K. His research interests include power electronics control, distributed power electronics systems, and fieldbus communication.

HAO MA (Senior Member, IEEE) received the B.S., M.S., and Ph.D. degrees in electrical engineering from Zhejiang University, Hangzhou, China, in 1991, 1994, and 1997, respectively.

Since 1997, he has been a Lecturer, an Associate Professor, and a Professor with Zhejiang University. From 2007 to 2008, he was a Delta Visiting Scholar with the North Carolina State University, Raleigh, NC, USA. He is currently the Vice Dean of ZJU–UIUC Institute. He has authored two books and authored or coauthored over 200 technical papers. His current research interests include advanced control in power electronics, wireless power transfer, fault diagnosis of power electronic circuits and systems, and application of power electronics.

Dr. Ma was an AdCom Member of the IEEE Industrial Electronics Society and the Technical Program Chair of the IEEE ISIE 2012, IEEE PEAC 2014, and IEEE PEAC 2018. He is currently the Director of the Academic Committee, China Power Supply Society. He is an Associate Editor of the IEEE JOURNAL OF EMERGING AND SELECTED TOPICS IN POWER ELECTRONICS and the *Journal of Power Electronics*.

XIANGNING HE (Fellow, IEEE) received the B.Sc. and M.Sc. degrees from Nanjing University of Aeronautical and Astronautical, Nanjing, China, in 1982 and 1985, respectively, and the Ph.D. degree from Zhejiang University, Hangzhou, China, in 1989.

In 1991, he obtained a fellowship from the Royal Society of U.K., and conducted research at Heriot-Watt University, Edinburgh, U.K., as a Postdoctoral Research Fellow, for two years. In 1994, he joined Zhejiang University as an Associate Professor. Since 1996, he has been a Full Professor with the College of Electrical Engineering, Zhejiang University. His research interests include power electronics and their industrial applications.

Dr. He is a fellow of the Institution of Engineering and Technology (formerly IEE), U.K. He has been appointed as an IEEE Distinguished Lecturer with the IEEE Power Electronics Society, in 2011.

● ● ●